

Soft X-ray imaging with coherence tomography in the water window spectral range using high-harmonic generation

Julius Reinhard ^{1,2,*}, Felix Wiesner ^{1,2,†}, Themistoklis Sidiropoulos ³, Martin Hennecke ³,
Sophia Kaleta ^{1,2}, Julian Späthe ¹, Johann Jakob Abel¹, Martin Wünsche ^{1,2,4}, Gabriele Schmidl⁵,
Jonathan Plentz ⁵, Uwe Hübner⁵, Katharina Freiberg ⁶, Jonathan Apell^{6,7}, Stephanie Lippmann ⁸,
Matthias Schnürer³, Stefan Eisebitt ^{3,9}, Gerhard G. Paulus ^{1,2}, Silvio Fuchs ^{1,2,10*}

¹Institute of Optics and Quantum Electronics, Friedrich Schiller University Jena, Max-Wien-Platz 1, Jena, 07743, Germany

²Helmholtz Institute Jena, GSI Helmholtzzentrum für Schwerionenforschung, Fraunhoferstr. 8, Jena, 07743, Germany

³Max-Born-Institut für Nichtlineare Optik und Kurzzeitspektroskopie, Max-Born-Straße 2A, Berlin, 12489, Germany

⁴Indigo Optical Systems GmbH, Moritz-von-Rohr-Str. 1a, Jena, 07745, Germany

⁵Leibniz Institute of Photonic Technology (Leibniz-IPHT), Albert-Einstein-Str. 9, Jena, 07745, Germany

⁶Otto Schott Institute of Materials Research Friedrich Schiller University Jena, Lödtergraben 32, Jena, 07743, Germany

⁷Institute of Materials Science and Engineering, Chemnitz University of Technology, Erfenschlager Str. 73, Chemnitz, 09125 Germany

⁸Institute of Applied Physics, Friedrich Schiller University Jena, Albert-Einstein-Str. 15, Jena, 07745 Germany

⁹Institute for Optics and Atomic Physics, Technische Universität Berlin, Straße des 17. Juni 135, Berlin, 10623 Germany

¹⁰Laserinstitut Hochschule Mittweida, University of Applied Science Mittweida, Technikumplatz 17, Mittweida, 09648 Germany

[†]These authors contributed equally to this work.

*Correspondence: julius.reinhard@uni-jena.de, silvio.fuchs@hs-mittweida.de

ABSTRACT

High-harmonic generation (HHG) is used as a source for various imaging applications in the extreme ultraviolet spectral range. It offers spatially coherent radiation and unique elemental contrast with the potential for attosecond time resolution. The unfavorable efficiency scaling to higher photon energies prevented the imaging application in the soft X-ray range so far. In this work we demonstrate the feasibility of using harmonics for imaging in the water window spectral region (284 eV to 532 eV). We achieve nondestructive depth profile imaging in a heterostructure by utilizing a broadband and noise-resistant technique called soft X-ray Coherence Tomography (SXCT) at a high-flux lab-scale HHG source. SXCT is derived from Optical Coherence Tomography, a Fourier based technique, that can use the full bandwidth of the source to reach an axial resolution of 12 nm in this demonstration. The employed source covers the entire water window, with a photon flux exceeding 10^6 photons/eV/s at a photon energy of 500 eV. We show local cross sections of a sample consisting of Aluminium oxide and Platinum layers of varying thickness on a Zinc oxide substrate. We validate the findings with scanning and transmission electron microscopy after preparation with focused ion beam milling.

INTRODUCTION

High-harmonic generation (HHG) has proven to be an exceptional source for nanoscale extreme ultraviolet (EUV) imaging due to its laser-like properties and small laboratory footprint¹⁻³. In particular, coherent imaging methods such as ptychography benefit from the high spatial coherence and have demonstrated their remarkable potential in recent years achieving wavelength-scale resolution⁴⁻⁷. In addition, the strong elemental contrast opens up a wide field of applications from semiconductor studies⁸ and mask inspection⁹ to biological samples¹⁰⁻¹². Even buried structures can be examined using EUV light from HHG sources¹³⁻¹⁵. However, the penetration depth is severely limited by the strong absorption of most materials.

Further decreasing the wavelength to the soft X-ray (SXR) range would not only decisively increase the penetration depth for a great variety of materials, but would also enhance the resolution as demonstrated at synchrotron sources¹⁶. Especially the so-called water window (WW), defined by the absorption edges of carbon (≈ 284 eV or 4.4 nm) and oxygen (≈ 532 eV or 2.3 nm), is of particular interest due to its high contrast and penetration depth in many materials, e.g. biological materials¹⁷⁻¹⁹.

HHG-driven imaging in the soft X-ray or more specifically the water window spectral range has not yet been demonstrated, primarily for two reasons. On the one hand, the available photon flux of HHG sources in the SXR range is severely limited. Extending the HHG spectral range into the water window typically requires ultrafast driver lasers with wavelengths above $1 \mu\text{m}$. Unfortunately, this reduces the conversion efficiency of the process, which scales with $\sim \lambda^{-5 \dots -6}$ ²⁰. Therefore, SXR-HHG have only been used for various spectroscopic applications that exploit the femto- or even attosecond pulse lengths²¹⁻²³. On the other hand, the intrinsically broadband harmonic spectrum is not efficiently used by the established EUV imaging methods like Ptychography,

which typically require monochromatic light and consequently only use a small fraction of the available photon flux. Thus, intrinsically broadband imaging techniques are better suited for flux-limited HHG sources in the water window spectral range.

In this work, we demonstrate the feasibility of HHG-driven imaging in the water window by combining a cutting-edge WW-HHG source with a broadband and noise resistant technique called soft X-ray coherence tomography (SXCT). The HHG source is driven by a few-cycle 2.1 μm laser²⁴ and generates a broad spectrum covering the entire water window with more than 5×10^5 ph/eV/s at the oxygen K-edge (2.33 nm)²⁵. To our knowledge, no other HHG source was able to apply these photon numbers in experiments yet. Moreover, SXCT exploits the full bandwidth of the source to reconstruct depth structures with nanometer-scale axial resolution. This imaging technique is derived from spectral-domain optical coherence tomography (OCT,²⁶) and functions as a reflective method, enabling the investigation of structures on bulk materials such as microchips. It even enables the study of weakly reflective samples due to its Fourier-based nature, which provides exceptional noise resistance. Furthermore, three-dimensional information can be obtained by laterally scanning the sample.

We investigated a sample composed of an aluminum oxide layer and a platinum layer deposited on a zinc oxide substrate using SXCT. A cross-sectional image was obtained scanning across the edge of the buried platinum layer, achieving a depth resolution of 12 nm. To validate the axial structure and inhomogeneities detected with SXCT, we conducted scanning and transmission electron microscopy (SEM and TEM) following focused ion beam (FIB) milling.

HHG SOURCE AND SXR COHERENCE TOMOGRAPHY

The demonstration of HHG-driven water window imaging was enabled by a high-flux HHG source covering the entire water window spectral range^{24,25}. The source is based on an optical parametric chirped-pulse amplification (OPCPA) system, driven by a 500 W thin-disk laser to reach a central wavelength of 2.1 μm and an average power of 28 W at pulse duration of 27 fs. The beam is focused with a 750 mm lens into a helium gas cell, where the HHG process occurs. The resulting spectrum covers a broad spectral range from 200 eV to 600 eV, with a photon flux of 5×10^5 ph/eV/s at the oxygen K-edge at ≈ 532 eV²⁵. The HHG spectrum which was used for the SXCT measurements is shown in Fig. 1.a.

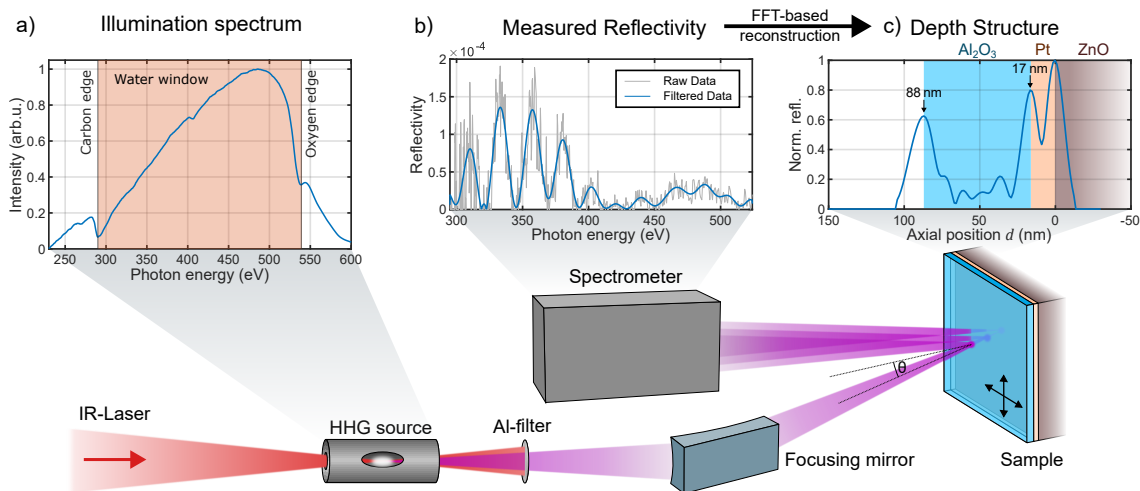


Figure 1: Illumination spectrum, measured sample reflectivity, and reconstructed depth structure arranged on top of a schematic representation of the setup. a) The illumination spectrum spans the entire water window spectral range. It is generated with high-harmonic generation driven by a few-cycle 2.1 μm laser. The spectrum is shaped by aluminium absorption filters, which contain oxides as well as carbon deposits. These features result in the strongly pronounced absorption edges of oxygen and carbon, which define the water window boundaries. b) The SXR light is focused onto the sample with a toroidal mirror. It is reflected at the various interfaces within the sample, leading to intensity modulations in the reflected spectrum due to interference. The high roughness of the sample leads to a significant reduction in reflectivity, resulting in a very noisy raw signal (grey). The signal relevant for the reconstruction was filtered out using a low-pass Fourier filter (blue). c) The depth structure of the sample was retrieved using the Fourier based SXCT algorithm. Three interfaces are reconstructed, which correspond to two layers with a thickness of 71 nm and 17 nm respectively on top of the substrate. By scanning across the sample, additional lateral information can be obtained.

Soft X-ray coherence tomography (SXCT) extends optical coherence tomography (OCT) to shorter wavelengths and broader spectral ranges, enabling high-resolution imaging in the soft X-ray regime. The axial resolution Δd is independent of the focusing geometry. Instead it is defined by the coherence length $l_c = \lambda^2 / \Delta \lambda$, i.e. a shorter wavelength and broader spectrum lead to higher axial resolution. With commercial OCT systems working in the infrared spectral range, axial resolutions of a few micrometers are achieved²⁷. In recent years,

XUV coherence tomography (XCT), the extreme ultraviolet descendant of OCT, was established in the silicon transmission window between 30 eV and 100 eV^{14,28–30}. This enabled an axial resolution of ≈ 15 nm, which has been demonstrated in a laboratory setup using HHG³¹.

SXCT is implemented as a common-path Fourier-domain OCT variant^{13,32}, in which the sample’s spectral response is detected by a spectrometer without the use of a beam splitter. Instead, the separation of the illumination and reflected beam is achieved through an oblique incidence angle. Consequently, the axial resolution Δd additionally depends on the incidence angle θ relative to the surface normal, following $\Delta d = \lambda^2 / (\Delta \lambda \cos \theta)$. In order to enhance the reflectivity and thereby increase the signal strength, particularly at short wavelengths, larger incidence angles can be utilized. However, this results in a slightly reduced axial resolution. In this experiment, we used an incidence angle of $\theta = 72^\circ$, enabling a maximum resolution of ≈ 10 nm for the spectral range from 284 eV to 532 eV.

The setup is schematically depicted in Fig. 1. A toroidal mirror focuses the SXR light from the HHG source onto the sample, forming an elliptical spot of $150 \mu\text{m} \times 300 \mu\text{m}$ due to $\theta = 72^\circ$. The light reflected from internal sample structures interferes with the light reflected from the surface, which serves as a reference in the common path SXCT scheme. This interference induces modulations in the spectrum of the reflected light, which are detected by a grating spectrometer. By measuring the incident spectrum (Fig. 1.a), the sample reflectivity (Fig. 1.b) can be determined.

The sample’s depth structure in the illuminated region is encoded in the spectral modulations of this reflectivity and can be reconstructed using a Fourier-based algorithm. The Fourier transform of the intensity reflectivity of the sample represents the autocorrelation of the axial sample structure, which is intrinsically ambiguous. However, the unambiguous axial structure can be reconstructed from the autocorrelation by employing a phase retrieval algorithm. In this work, we use a three-step one-dimensional phase retrieval algorithm originally developed for XCT¹⁴.

Due to the Fourier-based nature of the method, SXCT is highly resistant to noise, similar to the principle of lock-in amplifiers. Individual interfaces within the sample contribute to distinct modulation frequencies in the spectrum. Thus, broad-bandwidth noise can be efficiently filtered out, resulting in a high signal-to-noise ratio, as demonstrated in Fig. 1.b. The measured reflectivity of one sample position is shown in gray, while the reflectivity after low-pass Fourier filtering is shown in blue. Using this processed reflectivity as input, the established XCT reconstruction algorithm extracts the depth profile (Fig. 1.c). Each peak corresponds to an interface in the sample, where the reflections occur.

A cross-sectional or three-dimensional image of the sample can be obtained by laterally scanning in one or two dimensions while retrieving the axial structure point by point. As a consequence, the lateral resolution is independent of the axial resolution and defined by the size of the SXR probe on the sample which in our case was $150 \mu\text{m} \times 300 \mu\text{m}$.

EXPERIMENTAL RESULTS

SXCT cross section

We performed SXCT on a layered test sample, consisting of a ≈ 70 nm thick Al_2O_3 layer on a ZnO substrate. In a specific region of the sample, an additional Pt layer is buried below the Al_2O_3 with a thickness of ≈ 20 nm.

The measured reflectivity of a single lateral sample point is shown in Fig. 1.b, with values in the range of 10^{-4} . Compared to simulated data the measured reflectivity is more than one order of magnitude lower³³. The deviations can be attributed to differences in material density and non-negligible interface roughness. However, even with such a low reflectivity signal, particularly in comparison to the noise level, our reconstruction algorithm successfully retrieves the depth structure and resolves the position of the three interfaces, indicating a resolution of at least 17 nm (see Fig. 1.c).

Subsequently, we generate a cross-section (a so-called B-scan in OCT terminology) by measuring the depth structure (A-scan) at five different lateral positions as indicated with different colors in the schematic illustration of the sample (Fig. 2.a). Each position required an exposure time of 15 minutes.

The measured cross-section of the sample is presented in Fig. 2.b. Grayed-shaded areas represent interpolated regions between the scanning positions, which are indicated by the colored graphs and boundaries. Additional horizontal lines track the peak positions, which correspond to the interfaces in the sample. The depth structures were aligned such that the deepest interface (the substrate surface) is located at $d = 0$ nm. At lateral position $x = 0$ mm (blue curve) two peaks are visible: the Al_2O_3 surface (axial position $d = 71$ nm) and the $\text{Al}_2\text{O}_3/\text{ZnO}$ interface ($d = 0$ nm). As the lateral position x increases, a shift of the surface position becomes apparent. In addition, a broadening of the signal at the $\text{Al}_2\text{O}_3/\text{Pt}$ interface ($d = 15$ nm) becomes visible at $x = 0.8$ mm (orange). This is due to the presence of the buried Pt layer, which apparently does not have a sharp lateral edge, instead exhibiting a gradually increasing thickness. At $x = 1.2$ mm (yellow) the front ($d = 17$ nm) and back ($d = 0$ nm) of the Pt layer are clearly distinguishable. The Pt thickness further increases at $x = 1.6$ mm (purple) and $x = 2$ mm

(green) reaching 21 nm. The thickness of the Al_2O_3 -layer increases as well to 75 nm. Additionally, a decrease in signal strength is observed for larger x values, corresponding to an even lower reflectivity of 10^{-5} for the green signal. This can be attributed to increased roughness, which correlates with the growing Pt layer thickness. The roughness of the Pt layer also influences the roughness of the surface, further reducing the reflectivity.

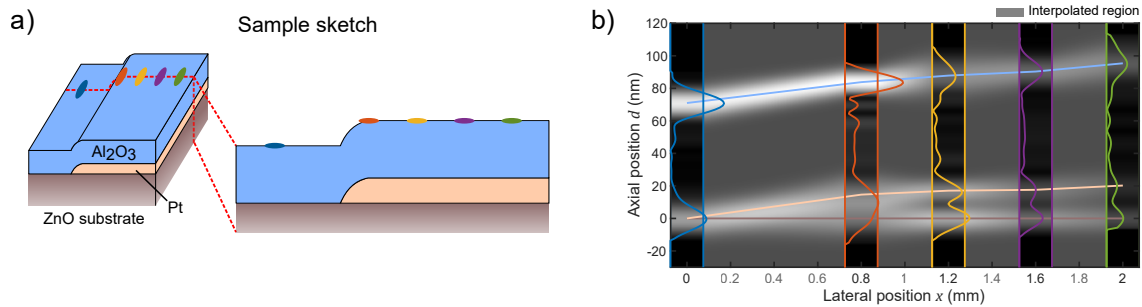


Figure 2: Cross-sectional imaging using SXCT: a) The investigated sample consists of a thin Al_2O_3 layer on a ZnO substrate, with buried Pt layer present in a specific region of the sample. b) A cross-section was obtained by scanning the sample at five different lateral positions. The size of the SXR-focus was $150\ \mu\text{m}$ in scanning direction. The grayed-out areas between the scanning positions are interpolated. The Al_2O_3 layer can be resolved throughout the sample with a varying thickness between 71 nm and 75 nm. In addition, the thinner buried Pt structure behind the edge can also be resolved with increasing thickness between 17 nm and 20 nm. At the second position (orange) the comparatively large SXR focus averages over a varying Pt thickness, leading to a broadened signal.

The peak positions were determined by Gaussian fitting of the depth structure at the scanning positions. This also revealed a FWHM of the $\text{Al}_2\text{O}_3/\text{Pt}$ interface at the yellow scanning position ($x = 1.2\ \text{mm}$, $d = 17\ \text{nm}$) of 12 nm, which defines the achieved resolution. For the purple ($x = 1.6\ \text{mm}$) and green scanning position ($x = 2\ \text{mm}$) the width increased to 15 nm, indicating a thickness variation of the Pt layer of $\pm 1.5\ \text{nm}$ in the illuminated region.

Validation with electron microscopy

We verified the SXCT results by performing scanning and transmission electron microscopy (SEM/TEM) investigations of the sample after FIB preparation. We compared three positions with corresponding SXCT scan positions: Al_2O_3 on substrate (blue position and blue frame in Fig. 3), Al_2O_3 with buried Pt (green) and close to the edge (orange). For all three positions, we prepared FIB cross sections and imaged them using SEM. In addition, we extracted a thin lamella with a width of $\approx 5\ \mu\text{m}$ from the $\text{Al}_2\text{O}_3/\text{Pt}$ position (green) and investigated it with TEM (Fig. 3.c). To protect the sample surface during FIB preparation, the sample was coated with gold and platinum after SXCT measurements. Details can be found in the Methods section.

A large field of view from the FIB cross section at the green position is presented in Fig. 3.b. It can be clearly seen from the granular structure that the platinum grows in columns and does not form a homogeneous layer. As a result, the layer exhibits a high roughness. On top of this, the $\text{Al}_2\text{O}_3/\text{Au}$ interface appears blurred (see also the enlarged area of the SEM image in Fig. 3.f), indicating the transition of roughness from the buried Pt layer to the surface, which further reduces the reflectivity.

The reasons for columnar growth of platinum can be attributed to two main factors. On the one hand, these are the deposition conditions, specifically the deposition pressure (Ar pressure) and temperature of the substrate surface (Thornton's model³⁴). On the other hand, it is the growth of platinum on an oxide surface, which can be described as island growth (Volmer-Weber growth mode³⁵). This combination results in a highly inhomogeneous vertical growth, particularly in the case of very thin layers. A TEM investigation at the same position (Fig. 3.c) confirms the non-negligible roughness of the Pt layer.

The lower part of Fig. 3 shows SEM images at three different lateral positions, enabling a direct comparison with the corresponding SXCT depth profiles. The SEM images were aligned, such that the ZnO/ Al_2O_3 or ZnO/Pt interface is at $d = 0$. As expected, no Pt is visible in the blue position (Fig. 3.d) and a sharp interface between the dark Al_2O_3 and the bright gold cover is observed at $d = 71\ \text{nm}$, which is in good agreement with the SXCT results. At the orange position (Fig. 3.e), the emergence of the Pt layer on top of the ZnO is visible in both the SEM image and the SXCT profile. The SXCT depth profile however, is integrated over a varying layer thickness due to the lateral extent of the SXR probe ($150\ \mu\text{m} \times 300\ \mu\text{m}$). For this reason, the interfaces cannot be resolved in this transition region of increasing Pt thickness. The enlarged image of the green position (Fig. 3.f), away from the boundary region, shows the fully formed Pt layer. The positions of the front and back of the Pt layer are in good agreement for SEM and SXCT.

From a series of ten measurements along the width of the TEM lamella (Fig. 3.c), a thickness of $21.5 \pm 1.1\ \text{nm}$ was determined for the platinum layer and $71.5 \pm 1.8\ \text{nm}$ for the Al_2O_3 layer. It is important to note that the error reflects the variation of the layer thickness across the width of the TEM lamella, rather than the method's inaccuracy.

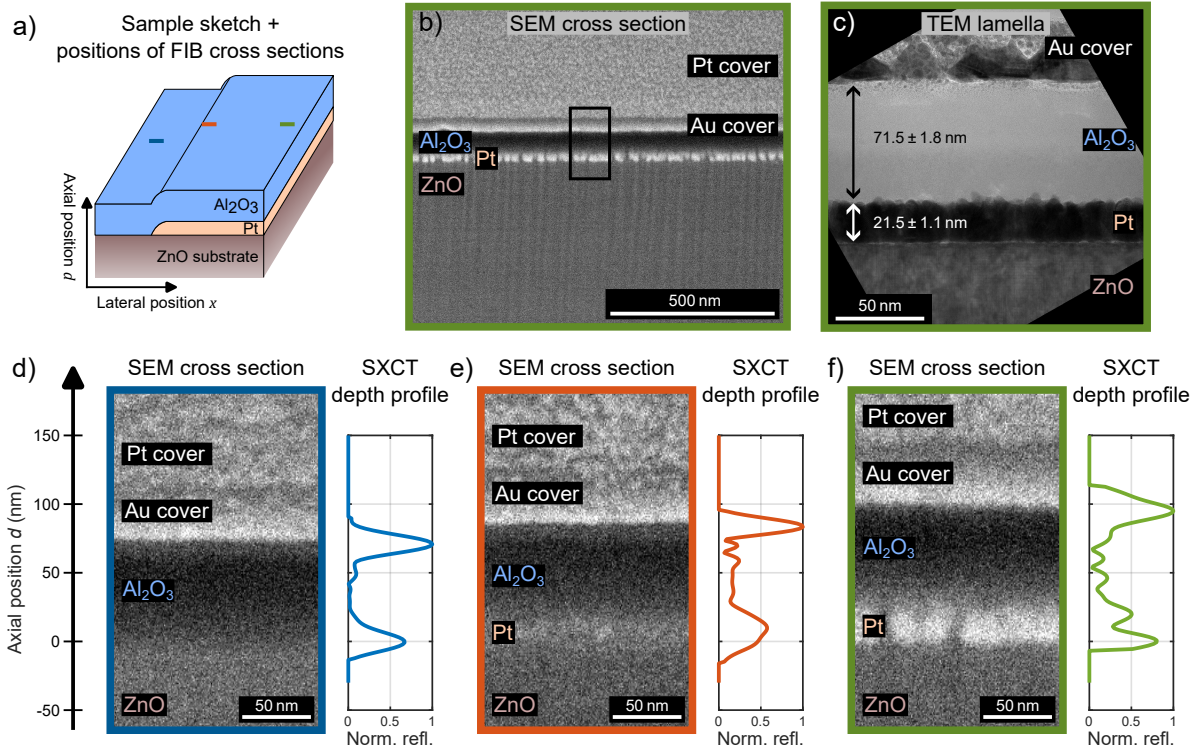


Figure 3: Validation of SXCT results with electron microscopy. a) Three regions on the sample are distinguished: Al_2O_3 on ZnO substrate (blue position), Al_2O_3 on Pt on ZnO substrate (green position) and the region in between with the Pt layer slowly forming (orange position). At each position a FIB cross section was made and compared to SXCT depth profiles. b) A SEM image of a FIB cross section at the green position, shows the Al_2O_3 and Pt layers, as well as the ZnO substrate and additional gold and platinum layers deposited in preparation for FIB milling. The bright Pt layer is easily recognizable and its high granularity and roughness is revealed. c) Section of the TEM lamella, prepared from the cross section shown in (b). The Al_2O_3 layer is visible on top of the inhomogeneous and rough Pt layer. Averaging over the full width of $5\ \mu\text{m}$, axial distances of $71.5\ \text{nm}$ and $21.5\ \text{nm}$ could be confirmed for Al_2O_3 and Pt, respectively. d-f) FIB cross sections were made at different sample positions and compared to corresponding SXCT depth profiles. The positions of the interfaces are highly consistent. It is confirmed that the thickness of the Pt layer gradually increases, rather than having a sharp edge.

CONCLUSION AND OUTLOOK

In this work, we showed that imaging with high-harmonic generation (HHG) sources is feasible in the water window (WW) spectral range. This was achieved by combining an HHG source that spans the whole WW range up to the oxygen edge and the flux efficient and noise resistant method of soft X-ray coherence tomography (SXCT). We imaged the internal sample structure of a layer system consisting of Al_2O_3 and Pt layers with an axial resolution of $12\ \text{nm}$, which is close to the theoretical limit of $10\ \text{nm}$ for this spectral range. The results of non-destructive SXCT were in remarkable agreement with those obtained using established, but destructive, scanning and transmission electron microscopy (TEM), both in terms of absolute layer thickness (TEM: $21.5\ \text{nm}$, SXCT: $21\ \text{nm}$) and thickness variation (TEM: $1.1\ \text{nm}$, SXCT: $1.5\ \text{nm}$) for the buried Pt layer. The thickness variation or high roughness and therefore low reflectivity of the test sample demonstrate the method's applicability to real-world samples. For higher-reflectivity samples, even lower axial resolutions in the single-digit nanometer range can be achieved by using steeper angles of incidence. This was demonstrated for a highly reflective periodic sample using an incoherent laser-plasma source, achieving an axial resolution of $< 5\ \text{nm}$ ³⁶.

Overall, our results represent an important first step towards exploiting the potential of water window harmonics for non-destructive imaging. Soft X-ray coherence tomography (SXCT) offers a valuable approach for studying materials whose absorption is too strong in the extreme ultraviolet (EUV) range. Simultaneously it provides strong elemental contrast, even for low-Z materials, a common challenge encountered in conventional TEM methodologies. In the EUV range, XCT has already been applied to material identification as well as the reconstruction of roughness and layer thicknesses well below the resolution limit²⁸. These approach can be extended into the SXR range, enabling further advancements. Cross-sectional imaging with HHG radiation will also facilitate the study of dynamic effects in buried layers with high spatial and femto- or even attosecond temporal resolution³⁷. Additionally, ongoing advancements in ptychographic algorithms aim to leverage broad spectra more effectively³⁸. Together with the development of even more powerful HHG sources, these innovations pave the way for future applications in the water window.

MATERIALS AND METHODS

Experimental Setup

The soft X-ray spectra were acquired using a combined $\theta - 2\theta$ reflectometry and spectroscopy setup, enabling transmission and reflection geometries for θ angles of $45^\circ - 90^\circ$. The soft X-rays were provided by a laboratory light source based on high-harmonic generation, operated with the noble gas helium (≈ 2.2 bar gas pressure). The HHG process was driven by $2.1 \mu\text{m}$, 27 fs (FWHM) infrared pulses generated via optical parametric chirped-pulse amplification (OPCPA). The OPCPA system features a monolithic concept, deriving the seed and pump pulses for the OPA stages from the same 500 W thin-disk pump laser (TRUMPF Scientific Lasers Dira 500-10), using a $2.1 \mu\text{m}$ front-end (Fastlite) for signal generation^{24,25}. The system delivers pulses with 10 kHz repetition rate at an average power of 28 W, which are focused into a helium gas cell to generate p-polarized ≤ 27 fs soft X-ray pulses covering a continuous spectrum from 200 to 600 eV. The resulting photon flux is $\approx 5 \times 10^5$ ph/eV/s @ O K-edge, $\approx 10^6$ ph/eV/s @ Ti L-edge and $\approx 6 \times 10^6$ ph/eV/s @ C K-edge, determined using a grating- and CCD-based spectrometer with absolute sensitivity calibration by the German metrology institute (PTB). The broadband pulses are focused onto the sample upon reflection by a toroidal mirror, leading to a footprint of the focal spot of $150 \times 300 \mu\text{m}^2$ (FWHM) for an angle of 72° to the surface normal. After reflection by the sample, the spectrum is dispersed by a reflection variable line spacing (VLS) grating (Hitachi 001-0450, 2400 l/mm central line density) and recorded on a CCD camera (Greateyes GE 2048 512 BI).

Data analysis

A reference spectrum was recorded prior to the linescan by moving the sample out of the beam path and aligning the spectrometer to the transmitted radiation. Calibration was done by fitting the grating equation to the carbon, nitrogen and oxygen edges visible in the spectra. We then applied offset correction, interpolation into the photon energy domain, and denoising to the recorded spectra, as explained below. The impact of these processing steps on the reflectivity and sample autocorrelation is shown in Fig. 4.

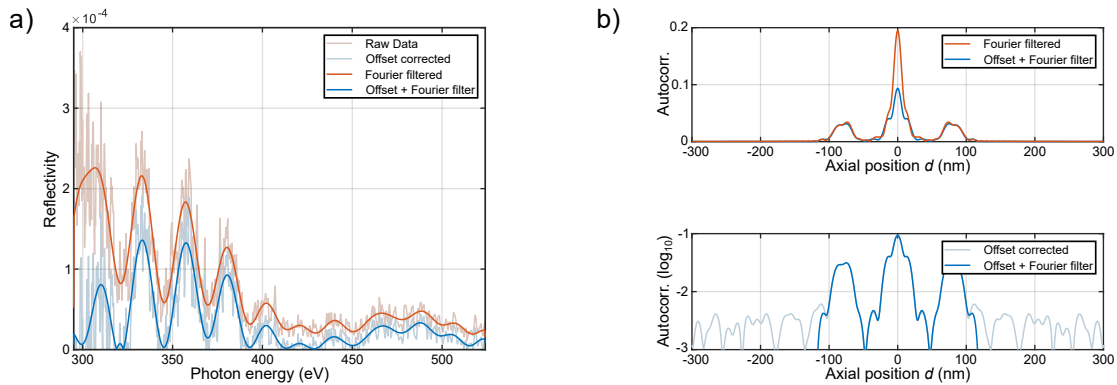


Figure 4: Denoising and offset correction of measured reflectivity data for reconstruction. a) The reflectivity is calculated by dividing the reflected spectrum of the sample by the illumination spectrum. The raw reflectivity gained this way is shown in gray. To denoise the data and eliminate high frequency modulations, a Fourier filter is applied, i.e. all values above or below ± 120 nm in the spatial domain are set to zero (red curve). Additionally, a background correction is applied, by subtracting a constant offset in the wavelength domain (blue). b) Autocorrelation of the sample structure with linear and logarithmic y-axis. The offset correction reduces the signal at zero depth in the autocorrelation as shown in the top figure. The bottom figure displays the applied Fourier filter, eliminating all signal above 120 nm.

The low reflectivity and incoherently scattered radiation from the inhomogeneous sample cause a significant offset in the measured reflectivity. In the sample autocorrelation this corresponds to an increased signal at zero depth. The phase retrieval relies on the correct correlation between the different features in the sample's autocorrelation. Therefore an offset in the sample reflectivity prevents convergence of the phase retrieval. The effects of the offset correction on the sample reflectivity and autocorrelation are shown in Fig. 4.a) and b). In this work, we assume a constant offset on the camera, i.e. in wavelength. We find that applying an offset subtraction of 0.27 Cts/s yields good results for all points of the linescan except for the point directly at the transition between Pt and Al_2O_3 , where a significantly larger offset is observed and a correction by 0.54 Cts/s is needed. The reason for this is the laterally inhomogeneous sample within the focal spot. The reflectivity is averaged over parts with a varying thickness of the Pt layer.

Due to the nonlinear relation between wavelength and photon energy $\lambda \propto 1/E$ the varying energy width of the camera pixels needs to be corrected by dividing by the energy spacing of the grid ΔE . The sample reflectivity is obtained by dividing the reflected spectrum of the sample by the reference spectrum.

Denoising of the reflectivity is performed by applying a low pass filter in the Fourier domain. This is equivalent to cutting off all signal that lies outside of the sample autocorrelation in depth domain, as can be seen in Fig. 4.b).

The interpolation of the SXCT cross section (Fig. 2.b) was based on Gaussian curve fitting. For each lateral position Gaussian curves were fitted to the peaks corresponding to the interface positions. The parameters of the curves (position, width and amplitude) were linearly interpolated between the lateral positions and used to plot the cross-section. For the second scan position (orange, $x = 0.8$ mm) three Gaussians were fitted to describe the broadened peak between $d = -10$ nm and $d = 20$ nm. One Gaussian corresponds to the substrate surface at $d = 0$ nm, while the other two are used to describe the varying thickness of the Pt layer. The mean value of these two positions is considered as the average position of the Pt/Al₂O₃ interface at $x = 0.8$ mm.

Electron microscopy

Cross sections were prepared using focused ion beam (FIB) milling in an FEI Helios Nanolab 600i dual-beam scanning electron microscope. The sample surface was protected by deposition of protective Au and Pt layers prior to FIB preparation. Cross sections were milled using an ion beam operating at 30 kV and 2.5 nA. SEM images were acquired using a secondary electron detector.

Cross section lamellae for transmission electron microscopy (TEM) were prepared using FIB and transferred to a Cu grid before applying the final thinning. Ion beam acceleration voltage and beam current were reduced down to 5 kV and 15 pA using stage tilts of 50.5° to 53.5°. TEM bright-field imaging was performed using a JEOL NEOARM 200F instrument.

Sample preparation

The platinum (Pt) and aluminium oxide (Al₂O₃) layers were deposited on a 10 × 10 mm² and 1 mm thick ZnO substrate. The Pt coating was deposited using a sputter coater with Ar as the sputtering gas. The base pressure was 6×10^{-2} mbar and the Ar pressure was 2×10^{-1} mbar. A rate of approximately 0.14 nm/s, a voltage of 1.3 kV and a current of 14 mA were used.

The deposition of aluminium oxide (Al₂O₃) has been performed using the atomic layer deposition (ALD) at a temperature of 225°C with 500 cycles. Each cycle took 70 ms. Trimethylaluminium (TMA) was the precursor for the vapor phase deposition.

To create two halves with different layer stacks on the substrate, a mask was used that was removed according to the coating sequence.

DATA AVAILABILITY

The raw spectra used in this experiment are available from the authors upon reasonable request.

ACKNOWLEDGMENTS

Thanks to Annett Gawlik and Uwe Brueckner from Leibniz IPHT for the deposition of Pt and Al₂O₃. Funding by ERDF in the project NanoMovie to develop and set up the HHG source at the Max Born Institute is gratefully acknowledged by S.E. This work was supported by the German Research Foundation (grant number PA 730/13-1); European Social Fund (ESF) with Thüringer Aufbaubank (2018FG008, 2015FG0094), and Bundesministerium für Bildung und Forschung (VIP “X-Coherent”).

AUTHOR CONTRIBUTIONS

J.R., F.W., S.F. and G.G.P. conceived the experiment. T.S., M.H., M.S. and S.E. conceived the laser system and HHG source and set up the experiment. J.R., F.W., S.K., J.S., T.S. and M.H. conducted the experiment. F.W. and J.R. analysed the data with supervision from S.F. and G.G.P.. The authors F.W., S.F., J.J.A., M.W. and J.R. developed the methodology. G.S., J.P. and U.H. prepared the sample. K.F., J.A. and S.L. performed the FIB milling and electron microscopy measurements. The manuscript was written by J.R., F.W. and S.F. All authors provided critical feedback on the research and the paper.

AUTHOR COMPETING INTERESTS

The authors declare no competing interests.

REFERENCES

- [1] Ferray, M. *et al.* Multiple-harmonic conversion of 1064 nm radiation in rare gases. *Journal of Physics B: Atomic, Molecular and Optical Physics* **21**, L31 (1988).
- [2] Popmintchev, T. *et al.* Bright coherent ultrahigh harmonics in the keV x-ray regime from mid-infrared femtosecond lasers. *Science* **336**, 1287–1291 (2012).
- [3] Klas, R. *et al.* Ultra-short-pulse high-average-power megahertz-repetition-rate coherent extreme-ultraviolet light source. *Photonix* **2**, 1–8 (2021).
- [4] Thibault, P. *et al.* High-resolution scanning x-ray diffraction microscopy. *Science* **321**, 379–382 (2008).
- [5] Loetgering, L., Witte, S. & Rothhardt, J. Advances in laboratory-scale ptychography using high harmonic sources. *Optics Express* **30**, 4133–4164 (2022).
- [6] Eschen, W. *et al.* Material-specific high-resolution table-top extreme ultraviolet microscopy. *Light: Science & Applications* **11**, 117 (2022).
- [7] Gardner, D. F. *et al.* Subwavelength coherent imaging of periodic samples using a 13.5 nm tabletop high-harmonic light source. *Nature Photonics* **11**, 259–263 (2017).
- [8] Tanksalvala, M. *et al.* Nondestructive, high-resolution, chemically specific 3d nanostructure characterization using phase-sensitive evu imaging reflectometry. *Science Advances* **7** (2021). URL <http://dx.doi.org/10.1126/sciadv.abd9667>.
- [9] Porter, C. L. *et al.* Soft x-ray: novel metrology for 3d profilometry and device pitch overlay. *Metrology, Inspection, and Process Control XXXVII* **12496**, 412–420 (2023).
- [10] Zürich, M. *et al.* Cancer cell classification with coherent diffraction imaging using an extreme ultraviolet radiation source. *Journal of Medical Imaging* **1**, 031008 (2014). URL <https://doi.org/10.1117/1.JMI.1.3.031008>.
- [11] Baksh, P. D. *et al.* Quantitative and correlative extreme ultraviolet coherent imaging of mouse hippocampal neurons at high resolution. *Science Advances* **6**, eaaz3025 (2020).
- [12] Liu, C. *et al.* Visualizing the ultra-structure of microorganisms using table-top extreme ultraviolet imaging. *Photonix* **4**, 6 (2023).
- [13] Fuchs, S. *et al.* Nanometer resolution optical coherence tomography using broad bandwidth xuv and soft x-ray radiation. *Scientific Reports* **6**, 20658 (2016).
- [14] Fuchs, S. *et al.* Optical coherence tomography with nanoscale axial resolution using a laser-driven high-harmonic source. *Optica* **4**, 903–906 (2017).
- [15] Shanblatt, E. R. *et al.* Quantitative chemically specific coherent diffractive imaging of reactions at buried interfaces with few nanometer precision. *Nano Letters* **16**, 5444–5450 (2016).
- [16] Shapiro, D. A. *et al.* An ultrahigh-resolution soft x-ray microscope for quantitative analysis of chemically heterogeneous nanomaterials. *Science Advances* **6**, eabc4904 (2020).
- [17] Schneider, G. Cryo x-ray microscopy with high spatial resolution in amplitude and phase contrast. *Ultramicroscopy* **75**, 85–104 (1998).
- [18] Coale, T. H. *et al.* Nitrogen-fixing organelle in a marine alga. *Science* **384**, 217–222 (2024).
- [19] Reinhard, J. *et al.* Laboratory-based correlative soft x-ray and fluorescence microscopy in an integrated setup. *Microscopy and Microanalysis* **29**, 2014–2025 (2023).
- [20] Tate, J. *et al.* Scaling of wave-packet dynamics in an intense midinfrared field. *Physical Review Letters* **98**, 013901 (2007).
- [21] Pertot, Y. *et al.* Time-resolved x-ray absorption spectroscopy with a water window high-harmonic source. *Science* **355**, 264–267 (2017).
- [22] Attar, A. R. *et al.* Femtosecond x-ray spectroscopy of an electrocyclic ring-opening reaction. *Science* **356**, 54–59 (2017).
- [23] Sidiropoulos, T. *et al.* Probing the energy conversion pathways between light, carriers, and lattice in real time with attosecond core-level spectroscopy. *Physical Review X* **11**, 041060 (2021).
- [24] Feng, T. *et al.* 27 W 2.1 μm OPCPA system for coherent soft x-ray generation operating at 10 kHz. *Optics Express* **28**, 8724–8733 (2020).
- [25] van Mörbeck-Bock, M. *et al.* High average power OPCPA MIR systems for coherent soft x-ray generation accessing absorption edges of metals. *High Power Lasers and Applications* **11777**, 11–16 (2021).
- [26] Huang, D. *et al.* Optical coherence tomography. *Science* **254**, 1178–1181 (1991).
- [27] Leitgeb, R. *et al.* Ultrahigh resolution Fourier domain optical coherence tomography. *Optics Express* **12**, 2156–2165 (2004).
- [28] Wiesner, F. *et al.* Material-specific imaging of nanolayers using extreme ultraviolet coherence tomography. *Optica* **8**, 230–238 (2021).
- [29] Wiesner, F. *et al.* Optical coherence tomography of van der Waals heterostructures using extreme ultraviolet light. *Advanced Materials Interfaces* 2400534 (2024).
- [30] Abel, J. J. *et al.* Non-destructive depth reconstruction of Al₂Cu layer structure with nanometer resolution using extreme ultraviolet coherence tomography. *Materials Characterization* **211**, 113894 (2024).
- [31] Nathanael, J. *et al.* Laboratory setup for extreme ultraviolet coherence tomography driven by a high-harmonic source. *Review of Scientific Instruments* **90**, 113702 (2019).
- [32] Vakhtin, A. B., Kane, D. J., Wood, W. R. & Peterson, K. A. Common-path interferometer for frequency-domain optical coherence tomography. *Applied Optics* **42**, 6953–6958 (2003).
- [33] Henke, B. L., Gullikson, E. M. & Davis, J. C. X-ray interactions: Photoabsorption, scattering, transmission, and reflection: E = 50–30,000 eV, Z = 1–92. *Atomic Data and Nuclear Data Tables* **54**, 181–342 (1993).
- [34] Thornton, J. A. High rate thick film growth. *Annual Review of Materials Science* **7**, 239–260 (1977).
- [35] Volmer, M. & Weber, A. Keimbildung in übersättigten gebilden. *Zeitschrift für physikalische Chemie* **119**, 277–301 (1926).

- [36] Wachulak, P., Bartnik, A. & Fiedorowicz, H. Optical coherence tomography (oct) with 2 nm axial resolution using a compact laser plasma soft x-ray source. *Scientific Reports* **8**, 8494 (2018).
- [37] Jarecki, J. *et al.* Ultrafast energy-dispersive soft-x-ray diffraction in the water window with a laser-driven source. *Structural Dynamics* **11**, 054303 (2024).
- [38] Shearer, B., Kapteyn, H., Binnie, I., Jenkins, N. W. & Murnane, M. Robust broadband ptychography algorithms for high-harmonic soft x-ray supercontinua. *Optics Express* **33**, 717–735 (2025).